Measurement of nanoparticle mass distributions by laser desorption/ionization time-of-flight mass spectrometry

2007 J. Phys.: Condens. Matter 19 176216

(http://iopscience.iop.org/0953-8984/19/17/176216)

IOP PUBLISHING JOURNAL OF PHYSICS: CONDENSED MATTER

J. Phys.: Condens. Matter **19** (2007) 176216 (13pp) doi:10.1088/0953-8984/19/17/176216

Measurement of nanoparticle mass distributions by laser desorption/ionization time-of-flight mass spectrometry

Jochen Maul

Institut für Physik, Staudingerweg 7, Johannes Gutenberg-Universität, 55128 Mainz, Germany

E-mail: jmaul@uni-mainz.de

Received 20 October 2006, in final form 14 March 2007
Published 30 March 2007
Online at stacks.iop.org/JPhysCM/19/176216

Abstract

In this paper, access to the mass distribution analysis of nanoparticles is described based on laser desorption/ionization and time of flight mass spectrometry. Two examples are given, demonstrating the accurate mass distribution analysis of nanoparticles fabricated both *ex situ* and *in situ* during the laser-assisted desorption process. The potentials and the limitations of the method are discussed, with special emphasis on carbonaceous clusters and molecules.

(Some figures in this article are in colour only in the electronic version)

1. Introduction

Nanoparticles have attracted much attention due to their potential for high-performance applications. They are of vital importance for future semiconductors [1] and electronics [2], for efficient catalysis [3] and for high-density magnetic storage devices [4]. Prominent examples are the single electron transistor [5], the quantum dot array [6] or catalysts to grow nanowires [7].

Whereas the bulk properties of materials do not change with the system size, the physical properties of nanoscale particles are strongly size-dependent. Furthermore, the size distribution of nanoparticles provides valuable information about their growth process. Thus, one important issue in nanoscience concerns the analysis of nanoparticle sizes and size distributions. Analytical access is given by bulk methods, such as gel permeation chromatography (GPC), vapour pressure and membrane osmosimetry, viscometry and the ultracentrifuge [8].

A complementary approach to obtain nanoparticle size distributions is given by microscopic methods, such as transmission electron microscopy (TEM) [9], photoemission electron microscopy (PEEM) [10] or scanning electron microscopy (SEM) as well as light scattering techniques on individual particles. From counting and subsequent size statistics

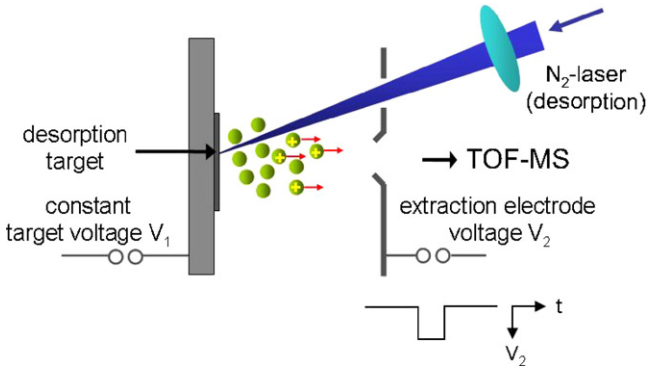

Figure 1. Illustration of the ion source setup. Ions produced by laser desorption/ionization from a target spot (potential V_1) are extracted into a TOF mass spectrometer by a subsequent electric field pulse applied to the extraction electrode (potential V_2).

evaluation of well identified particles, the size distribution can be reconstructed. However, these methods bear the risk of being size selective due to the identification process itself.

All methods cited above have the disadvantage of being time-consuming and—in the case of bulk methods—require a substantial quantity of the analyte. Mass spectrometric methods, in contrast, usually show a high sensitivity and allow for a quick analysis. Especially in case of spatially resolved mass spectrometry, the quantity needed for sampling can be kept at a minimum. The method presented in this article combines laser desorption/ionization in a small region of interest with mass spectrometry.

Since intense laser irradiation might introduce melting and vaporization in materials such as metals, special care has to be taken within laser desorption/ionization mass analysis in order to detect intact particles. In the present work, the analysis is restricted to carbonaceous particles which are robust with respect to melting: nanodiamonds which are suspended onto a substrate surface (section 3.1) and fullerenes which are produced *in situ* during the laser desorption process (section 3.2). Both types of sample exhibit lognormal mass distribution whose origin is elucidated in section 4. In case of the nanodiamond sample, accuracy of the mass distribution analysis is confirmed by a comparative TEM study. For the case of fullerenes in particular methodical questions are more intensely discussed in section 5.

The samples discussed cover a wide mass range from below 300 u to above 100 000 u and therefore motivate investigations on other (carbonaceous) clusters and nanoparticles, such as atmospheric dust and soot particles.

2. Experiment

2.1. Experimental setup

For mass distribution analysis of nanoparticles, a matrix assisted laser desorption/ionization-time-of-flight (MALDI-TOF) mass spectrometer (Bruker REFLEX III) was used. A schematic view of the ion source setup is shown in figure 1. Different samples were mounted onto commercial stainless steel target plates which were kept at a potential of 20 kV, and particles were released from the surface by nitrogen laser irradiation (Laser Science Inc., VSL-337 ND, $\lambda = 337$ nm, pulse duration $\sim$4 ns, maximum pulse energy $\sim$300 μJ). The distance between the target and extraction electrode is 2.5 mm.

Ions produced during the laser desorption/ionization process are subsequently extracted into a time-of-flight (TOF) spectrometer by means of a pulsed electric field applied to the extraction electrode (extraction potential switching from 20 to 18.9 kV; target potential 20 kV; rising edge ∼50 ns). The pressure in the whole chamber was kept at $\sim 10^{-7}$ mbar. Mass analysis was performed in the linear detection mode of a reflectron-type TOF spectrometer, which uses a microchannel plate (MCP) detector in combination with a 2 GHz transient recorder for data readout. The achievable spatial resolution of the setup was determined to <27 μm, and further experimental details are described in [11].

2.2. Nanodiamond samples

Two types of nanodiamond were investigated: synthetic ultradisperse diamonds and a cosmic diamonds fraction from the Allende meteorite which landed in Mexico in 1969.

Synthetic ultradisperse diamonds (UDDs, type 'CH7') were produced as dilute trace component during detonation of a composite explosive (trotyl/cyclotrimethylene-trinitramine, TNT/RDX) in a hermetic tank filled with inert gas (nitrogen, argon) of varied partial nitrogen pressures [12]. The detonation parameters, e.g. the nitrogen pressure and the TNT/RDX ratio, were optimized to increase the UDD yield. Subsequently the UDDs were obtained as solid residue after soot oxidation with perchloric acid.

Cosmic diamonds from the Allende meteorite (see e.g. [13] for an overview) were extracted from the meteorite samples by first dissolving the bulk material within a combined hydrochloric/hydrofluoric acid treatment. This was followed by dissolving sulfur using carbon disulfide as well as destroying organic compounds with Na-dichromate. The residues were then washed with distilled water, and perchloric acid was used to oxidize surviving graphitic carbon. Finally, using ammonium hydroxide, the diamond fractions were extracted as colloids. In some cases, an additional treatment with sulfuric acid was performed in order to dissolve additional oxidic minerals such as spinel ($MgAl_2O_4$).

For identification both nanodiamond samples were suspended in highly purified water ('Milli-Q water'), and several drops of the suspension were dried on a TEM copper grid coated with holey carbon film (Plano). The grid samples were then characterized by means of high-resolution transmission electron microscopy (HR-TEM, Philips TECNAI F30). TEM images from both nanodiamond samples are shown in figures 2(a) and (b).

2.3. Fullerene production

Fullerenes were produced during the laser desorption process from a glass carbon substrate (Sigradur G, HTW GmbH, Thierhaupten, Germany) coated with a dried droplet of 2,5-dihydroxy benzoic acid (DHB) dissolved in tetrahydrofurane (THF). Here, DHB is not used for its original purpose as a MALDI matrix but as an absorbing educt which undergoes a photochemical reaction to produce the fullerenes. The DHB/Sigradur system is especially suited for an efficient energy transfer of the laser light to the target since DHB exhibits a maximum absorption near the nitrogen laser wavelength of 337 nm [14]. In this experiment, fullerenes were obtained neither from pure glass carbon nor from DHB transferred on a steel target.

3. Results

This section is structured as follows: in subsection 3.1 the mass distribution analysis of two different nanodiamond samples is discussed. This *ex situ* analysis concerns readily formed

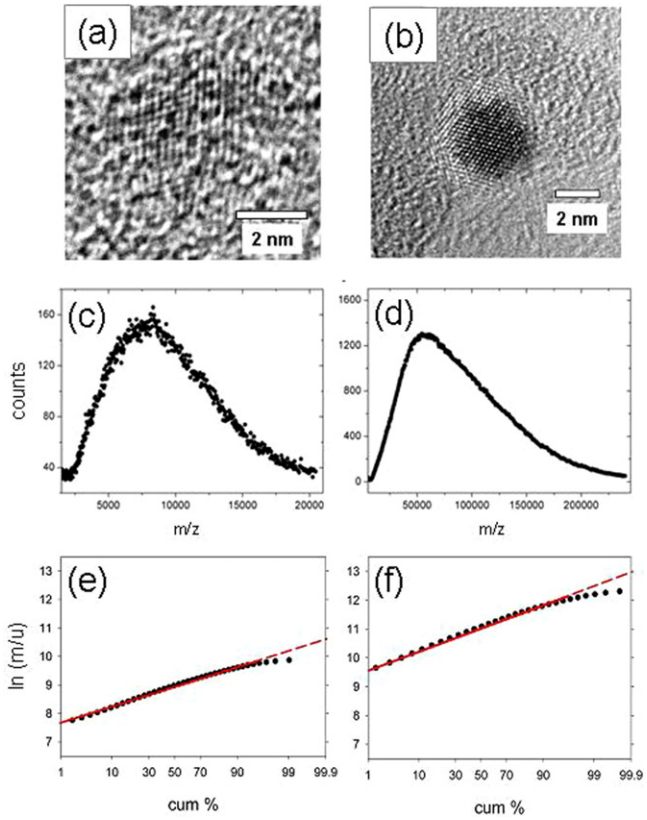

Figure 2. Mass distribution measurement of nanodiamond samples: (a) Allende meteorite and (b) synthetic diamond TEM images; (c), (d) laser desorption/ionization TOF mass spectra; (e), (f) cumulative representation of mass distributions for statistical analysis. The TEM images in (a) and (b) were kindly provided by van Aken.

particles in the extended mass range from 1000 u to 200 000 u. In subsection 3.2 the mass distributions of positive fullerene ions formed *in situ* during the laser desorption/ionization process are presented. Here, special emphasis is put on the parametric dependences of the growth process. This analysis concerns the low and medium mass range below 5000 u.

3.1. Nanodiamond mass distributions

Mass distributions of both nanodiamond samples were recorded by means of matrix-free laser desorption/ionization in combination with time-of-flight mass analysis. For this, the diamond samples were suspended with distilled water and dried on a stainless steel target plate. Near the desorption threshold measurements were performed for a conservative sample treatment during the laser-induced desorption/ionization process.

For desorption, the nitrogen laser was used in the moderate fluence range between 0.35 and 0.40 J cm^{-2}. Mass spectra were recorded in the linear detection mode of the reflectron-type TOF spectrometer. For each mass spectrum, 50 laser shots were applied to 12 different sample positions (i.e. 600 shots in total) for the release of nanoparticles on a target spot of $\sim$30 μm diameter. To reduce the number of data recorded by means of the built-in digital transient

recorder, 200 channels corresponding to a time segment of 100 ns were binned to obtain one averaged data point.

The binned mass spectra from the Allende diamonds and from the UDDs are shown in figures 2(c) and (d), respectively. All mass spectra are characterized by a steep rise at lower masses and a rather weak descent to higher masses. As known from previous TEM studies [15] in which individual cosmic diamonds were identified and subjected to statistical analysis, the statistics follows a lognormal distribution

$$\Lambda(r|\,\mu_r, \sigma_r^2) \;\propto \frac{1}{\sqrt{2\pi\,\sigma_r^2}\,r} \times \exp(-\,(\ln[r/nm] - \mu_r)^2/(2\,\sigma_r^2)) \tag{1}$$

where r is the particle radius, $\mu_r = \ln(\langle r/nm\rangle)$ is the logarithm of the median radius $\langle r\rangle$ and σ_r is a form parameter characterizing the asymmetry of the curve (the distribution becomes almost symmetric for $\sigma_r \to 0$, and is highly asymmetric for $\sigma_r > 1$). An extended statistical analysis of several types of nanodiamond sample is found in a previous article [16]. In the present work, more emphasis is put on methodological questions.

In order to compare size distributions with the related mass distributions, a special feature of the lognormal distribution has to be considered: a quantity which is connected to a lognormal variate by a power law also represents a lognormal variate. The relationship between mass m and radius r is given by a third power law, i.e. $m = \rho 4\pi r^3/3$ assuming spherical geometry in a simplified picture (ρ is the material density).

For quantitative analysis, the lognormal characteristics can be linearized by using the straight line representation $\ln(\xi) \to \xi\sigma + \mu$ with $\mu = \ln(m/u)$ in a cumulative probability plot (i.e. the accumulated percentage of the whole curve area is plotted as explained in [17, 18]). The linearized lognormal mass statistics are shown in figures 2(e) and (f). In both diagrams, linear fitting applies well. A value of $\langle m\rangle \sim 8000$ u is extracted for the Allende fraction, and a median mass of $\langle m\rangle \sim 65\,000$ u is obtained for the UDDs.

Furthermore, the extracted median mass values are in good agreement with the TEM reconstructions of the size distributions. The size distribution of the meteoritic sample has been determined by Daulton *et al* [19] using TEM. In that work, a median effective diameter of ∼2.8 nm was obtained for the Allende fraction. However, a significantly lower median diameter of $\langle d\rangle \sim 1.0$ nm was obtained by Fraundorf *et al* [20] for Allende diamonds. Using a density of 3.52 g cm^{-3} for crystalline diamond and assuming spherical diamond geometries, we calculate from our data a median effective diameter of ∼1.9 nm for Allende diamonds. In the case of the synthetic UDD sample, a median effective diameter of 3.9 nm is calculated from the median mass of 65 200 u. This is in good agreement with the size determination by Kuznetsov *et al* [12], where an average UDD diameter between 3.0 and 5.0 nm has been determined, depending on the specific nitrogen pressure and the specific TNT/RDX ratio during synthesis. In this way, the TEM measurements serve as a test for the accuracy of the method.

In a recent work by Lyon *et al* [21], matrix-assisted laser desorption/ionization (MALDI) in combination with TOF-MS was used to assess mass distributions of meteoritic nanodiamonds. The laser light introduces desorption and ionization by energy transfer from an organic matrix to the analyte. Good agreement with TEM data was likewise found. The advantage of MALDI-TOF is generally founded in the 'soft' desorption process without fragmentation. In our analysis, this soft desorption could be realized by laser irradiation close to the desorption threshold.

Since TEM particle counting experiments [19, 20] are based on the two-dimensional particle projection onto the substrate surface, some systematic uncertainties are involved during the translation to the corresponding particle volume. Therefore both the specific crystal structure and the orientation onto the TEM substrate surface need to be considered.

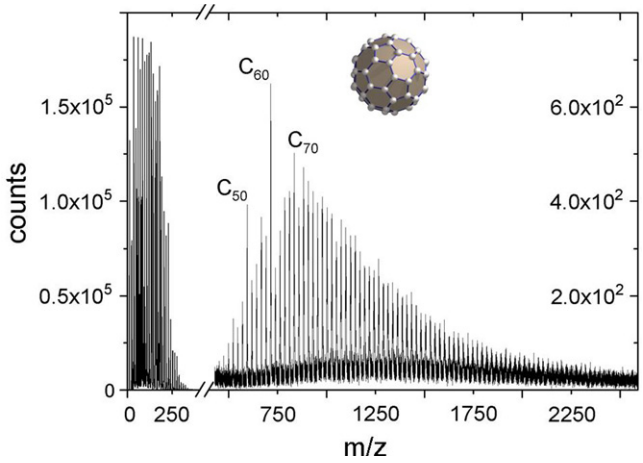

Figure 3. Mass spectrum of positive fullerene ions. The spectrum shows a bimodal structure with a gap around 400 u which separates the smallest carbon clusters from the fullerenes. Above the gap the 'magic' fullerenes C_{50}, C_{60} and C_{70} stand out by their overabundance compared to the residual fullerene distribution. The intersection in the gap was chosen for a better comparability of the different ion yields in both mass ranges (inset: sketch of the C_{60} molecule).

This problem is intrinsically circumvented by using mass spectrometry. Especially for laser desorption/ionization mass spectrometry (and in contrast to electrospray ionization mass spectrometry (ESI-MS), for example [22]) it is known that predominantly singly charged ions are produced which significantly simplifies the evaluation [23]. Methodological uncertainties in the laser desorption method, on the other hand, might arise from possible fragmentation of intact nanoparticles during the laser irradiation process at increased laser fluences, as well as from possible laser-induced fusion of individual nanoparticles.

3.2. Fullerene mass distributions

In this subsection, mass distributions of fullerene ions produced during the laser desorption/ionization process are analysed.

Figure 3 shows a positive carbon cluster ion mass spectrum with a typical bimodal structure generated from a laser-induced plasma as described in section 2.3. Small carbon clusters (masses $m < 400$ u) appear at each multiple carbon mass. They are separated from the fullerenes with even-only numbers of carbon atoms by a gap around the mass $m \sim 400$ u. In the complete fullerene mass range we exclusively observe singly charged ions as is depicted from the mass differences of 24 u between neighbouring peaks. This is further substantiated by the observation of integer mass differences between the isotopomer peaks between 500 u and 600 u, where the mass resolution allowed for a clear distinction of two neighbouring masses. For higher masses (i.e. above 1000 u), this distinction failed because of continuously decreasing mass resolution.

The statistical analysis of the fullerene mass comb from figure 3 is presented in figure 4, similar to the analysis presented in the previous subsection 3.1. First, the counts for each fullerene size N are extracted into a normalized histogram (figure 4(a)) where the total number of carbon atoms N is subtracted by the number of carbon atoms for the smallest configurationally allowed fullerene (20) [24]. This defines the modified cluster size

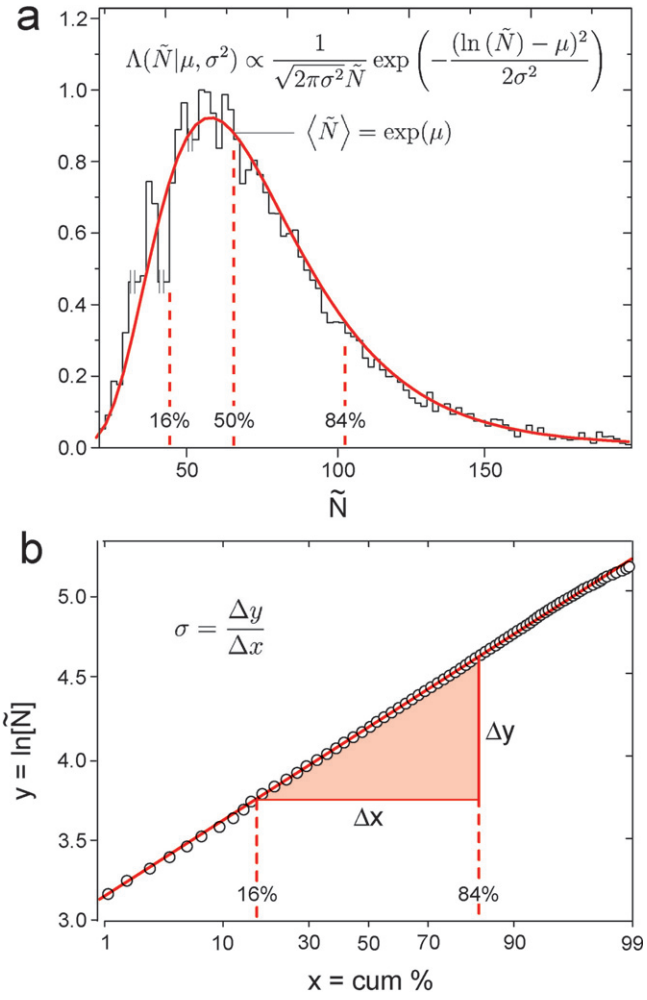

Figure 4. Statistical analysis of a fullerene mass spectrum. The normalized histogram in (a) shows the abundance of each fullerene size $\tilde{N}$ in figure 3 (see text for definition). The excess abundance of the 'magic' fullerenes C_{50}, C_{60} and C_{70} is thereby removed as indicated by the vertical intersections. A lognormal fitting curve is applied to the histogram data, and the values of 16%, 50% and of 84% of the integral area are marked by dotted lines. The 50% value directly translates into the median fullerene size $\langle\tilde{N}\rangle$ which is connected to the distribution parameter μ. The lognormal statistics is emphasized by the linearization given in (b). Here, the logarithm of the cluster size $\tilde{N}$ is shown against the cumulative fullerene frequency. The slope in this representation directly provides the shape parameter $\sigma = \Delta x/\Delta y$.

$\tilde{N} = N - 20$ which introduces a natural variate for the two-parameter lognormal distribution

$$\Lambda(\tilde{N}|\,\mu,\sigma^2) \;\propto \frac{1}{\sqrt{2\pi\,\sigma^2}\,\tilde{N}} \times \exp(-\,(\ln\tilde{N}-\mu)^2/(2\,\sigma^2)). \tag{2}$$

Here, the inherent offset of 20 atoms is referred to as a 'waiting point' in the statistics [17]. The dimensionless parameter μ is connected to the median size $\langle\tilde{N}\rangle$ of the lognormal distribution via $\langle\tilde{N}\rangle = \exp(\mu)$ (resp. $\langle N\rangle = \langle\tilde{N}\rangle + 20$).

The lognormal function Λ provides an excellent fitting to the fullerene distribution. The quality of the fitting curve is emphasized even more by the linearization given in figure 4(b).

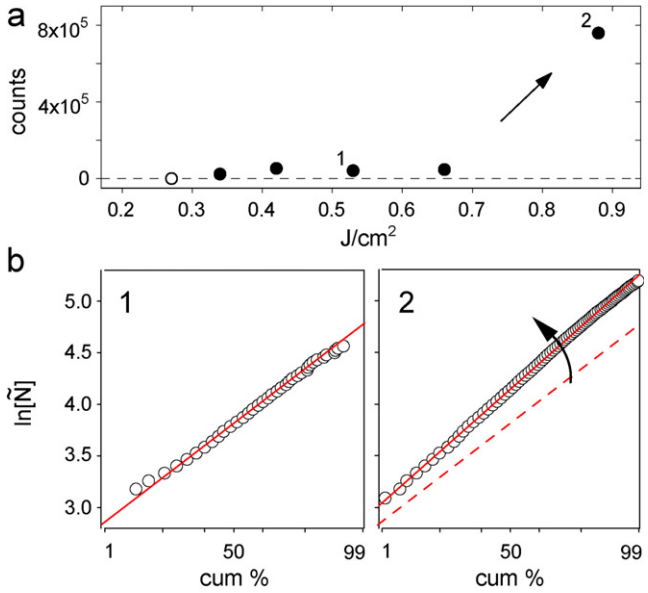

Figure 5. Correlation between fullerene ion yields and lognormal distribution parameters. (a) Fullerene ion yields obtained in the laser fluence regime below 1 J cm^{-2}. Beyond 0.2 J cm^{-2} first a moderate fullerene ion yield is observed in the mass spectrum (1) which abruptly increases above a threshold near 0.8 J cm^{-2} (2). The appearance of the threshold is also reflected within the cumulative probability plots in (b) by a rotation of the straight line around the lowest fullerene size. The delay time Δt between laser pulse and extraction pulse was chosen to 300 ns.

The parametric form of the straight line, $\xi \rightarrow \sigma\xi + \mu$, directly provides the statistical parameters $\sigma = \ln(1/2[\xi_{50\%}/\xi_{16\%} + \xi_{84\%}/\xi_{50\%}])$ and $\mu = \ln(\xi_{50\%})$, where $\xi_{16\%}$, $\xi_{50\%}$ and $\xi_{84\%}$ are depicted from the 16%, 50% and 84% values of the corresponding cumulative probabilities.

In order to obtain 'textbook statistics' such as presented in figure 4, an increased laser fluence for desorption was applied to create a dense and highly collisional plasma. In figure 5(a), the integral desorption yields for positive fullerene ions on a single ablation spot are given in dependence on the laser fluence. Moderate fullerene yields are obtained below ~0.8 J cm^{-2}, and a significant increase is observed above. As apparent from the lognormal cumulative plots given in figure 5(b), the desorption yield correlates with the mass span of the recorded fullerenes. Above this threshold, a denser plasma is released, giving rise to higher collision rates. This is reflected by an increase in the medium cluster size $\langle\tilde{N}\rangle$ (from 45.0 to 62.9), along with a change in the shape parameter from $\sigma = 0.40$ to $\sigma = 0.49$. This is also recognized from a rotation of the straight line around the lowest cluster size.

To depict the temporal evolution of lognormal fullerene growth, the time span Δt between the laser pulse and the pulsed ion extraction into the TOF analyser is varied (figure 6). For continuous ion extraction into the TOF spectrometer ($\Delta t = 0$) no fullerenes were recorded. With increasing time for growth, the median size is shifted from $\langle\tilde{N}\rangle = 65.5$ for $\Delta t = 300$ ns to $\langle\tilde{N}\rangle = 87.6$ for $\Delta t = 900$ ns. The asymmetry of the frequency curves diminishes, as is recognized from a decrease in the shape parameter from $\sigma = 0.43$ for $\Delta t = 300$ ns to $\sigma = 0.36$ for $\Delta t = 900$ ns. In the cumulative plots, the temporal evolution is accompanied by a rotation of the straight lines around the upper end of the distribution. This can be understood from two counteracting criteria, i.e. the vanishing of smaller fullerenes in favour of larger ones accompanied by a decrease in the total number of particles during coalescence. Thereby, two

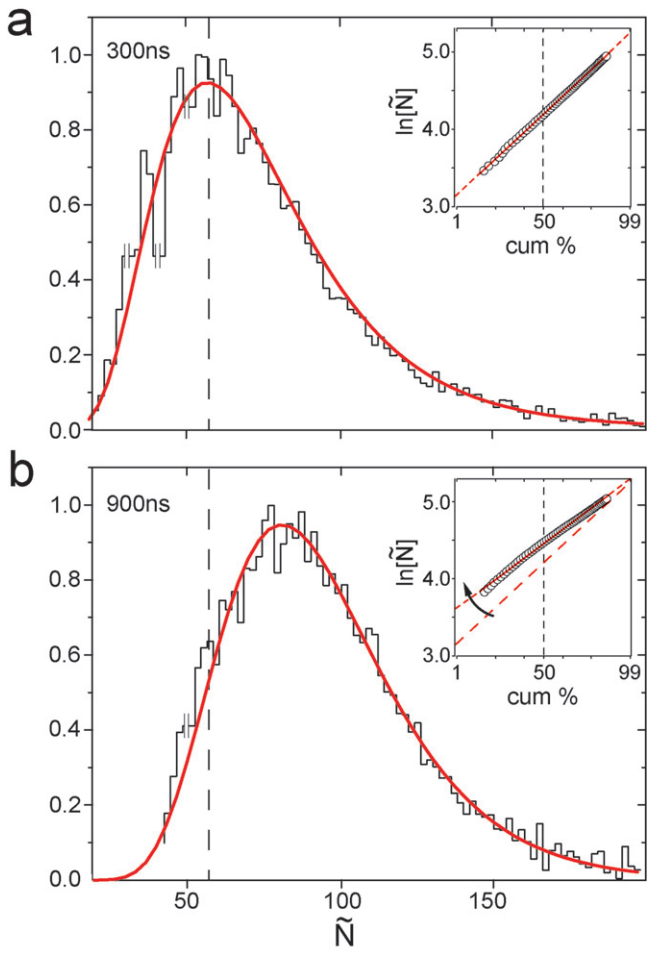

Figure 6. Temporal evolution of the fullerene growth process as observed from the size statistics. The histograms show fullerene size distributions obtained (a) 300 ns and (b) 900 ns after the desorption laser pulses. With increasing growth duration the distributions are shifted to higher cluster sizes. Simultaneously, the distribution asymmetry decreases as it is recognized from the shape of the lognormal fitting curves and from the corresponding straight lines in the cumulative plots (insets) which rotate about the highest cluster size. The laser fluence was chosen as 0.8 J cm^{-2}.

smaller particles vanish within an inelastic two-body collision to build one larger fullerene as it is also expressed by a decrease of the rate constants. Further details of the fullerene growth process have been published in a recent work [25]. It should be noted that a lognormal curve was used in [26] as a guideline to describe the carbon cluster anions mass spectrum, but without statistical analysis.

4. Origin of the lognormal size distribution

The statistical theory of the *logarithmo-normal* or simply *lognormal* size distribution was originally set down by McAlister in 1879 [27]. Since then, our theoretical understanding and

the range of applications have greatly increased, although it was believed for a long time that it is of less fundamental importance compared to the earlier formulated normal and binomial 'sister distributions'.

The lognormal distribution arises from a theory of elementary errors combined with a multiplicative process, just as the underlying change of growth is multiplicative rather than additive. In contrast to a constant (size-independent) growth process, where the particle radius r_j increases to the following time, resp. process, step $j+1$ by a constant value [17, 28],

$$r_{j+1} - r_j = k_j, \tag{3}$$

the origin of lognormal growth must be sought in a proportionate (size-dependent) growth of the variate r_j,

$$r_{j+1} - r_j = k_j r_j. \tag{4}$$

As a consequence, particle growth is accelerated for larger particle sizes at the expense of smaller ones. The lognormal statistics is well-known, e.g. for atmospheric aerosols [29] and snow crystals [30] merging onto inelastic collision.

In the case of nanodiamonds, this mechanism infers the accumulation of smaller nanodiamonds to larger ones. In contrast, this excludes 'onion-like' shell-by-shell growth.

In the case of fullerene cluster condensation, the size statistics emerges from the second-order reaction [31, 32] inferred from purely classical inelastic two-body collisions between two cluster species (I–J) and J in the laser-induced plasma to form the species I:

$$J + (I - J) \overset{K_1/K_{-1}}{\longleftrightarrow} I. \tag{5}$$

Here K_1 and K_{-1} denote the growth rate constants for both ways: one of both species J and (I–J) is positively charged to be accessible by the mass spectrometric detection.

Within this second-order reaction dynamic lognormal growth is deduced from the kinematic description provided by the Smoluchowski differential equation for the concentrations n_I, n_{I-J} and n_J of the corresponding species [33, 34]:

$$\frac{\mathrm{d}n_I}{\mathrm{d}t} = \frac{1}{2}\sum_{J=1}^{I-1} K_{J,I-J} n_I n_{I-J} - n_I \sum_{J=1}^{\infty} K_{I,J} n_J. \tag{6}$$

The Smoluchowski equation includes both coalescence of smaller species J and (I–J) to form the fullerene I (first term), and also continuative coalescence to larger species (second term).

Note that for fullerenes the index I takes even values only, starting with the geometric restriction of $I = 20$ carbon atoms per molecule. The lognormal distribution is obtained as the asymptotic solution of the Smoluchowski equation for reaction times Δt large compared to the inverse collision rate K ($\Delta t > 1/K$), and for large cluster sizes I [33]. The latter is intrinsically fulfilled for fullerenes. Furthermore, the rate constants $K_{I,J}$ need to be homogeneous of negative degree ω for arbitrary interacting species I and J [33], $K_{\lambda I,\lambda J} = \lambda^{2\omega} K_{I,J}$ ($\omega < 0$; $\lambda > 1$). This downscaling reflects the decrease in the cluster velocities for larger fullerenes onto each inelastic collision, thus lowering the collision rates with increasing mass.

Remarkably, the growth of fullerenes is not due to stepwise accumulation of single carbon atoms or the smallest carbon subunits, but follows an inelastic collision dynamics inferring all clusters are present in the plasma. In turn, this means a high degree of self-organization leading to the formation of larger hollow fullerene cages.

5. Experimental pitfalls

Recording mass distributions by means of laser desorption TOF-MS bears the risks of artefacts which have to be discussed on different levels.

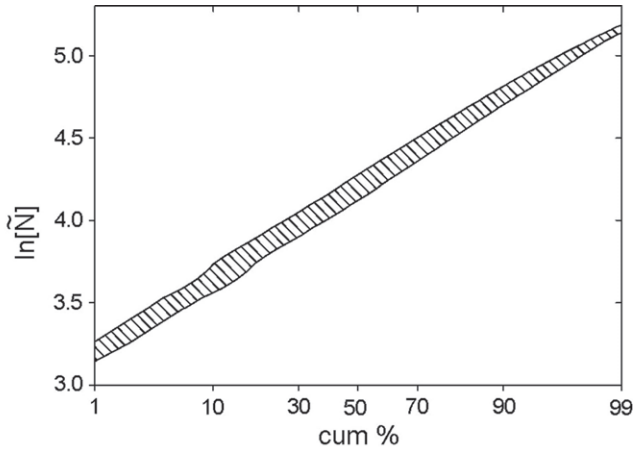

Figure 7. Error band for cumulative probability curves of fullerene ions obtained for different potential settings in the ion optical system. The laser fluence for fullerene production from the carbonaceous DHB substrate was 0.9 J cm^{-2}. Data from three different potential settings have been merged to connect the topmost, resp. lowermost, data points (see text for explanation).

Starting with ion production from the laser desorption/ionization process, different species present in the desorption plasma might have different ionization probabilities. This mainly holds for molecules of essentially differing chemical properties, but amounts to a minor degree for chemical homologues, such as (non-magic) large carbon clusters like fullerenes and nanodiamonds. In addition, the question of different desorption probabilities arises, especially in the case of phase separation. It is known, e.g. for alloys, that laser desorption can introduce thermal fractionation and lead to the preferred desorption of the less refractory constituent [35]. In case of layer-by-layer desorption this is of minor importance.

Secondly, mass-dependent transmission through the mass separating apparatus might occur. TOF spectrometers are, however, known for their supreme overall transmission near unity for all produced ions [36].

The final step of the ion mass detection appears particularly critical. In our setup, a MCP detector is used to record the ions. However, the ion detection probability in MCP detectors depends on the impact velocity of the ion [37, 38]. For mass distribution analysis over a wide mass range, all ions need to be accelerated to a sufficiently high a potential to guarantee detection of each ion hitting an individual channel.

In some mass spectrometers, fullerene ion distributions were obtained from acceleration potentials between 1 and 2 kV which was shown to be insufficient to avoid mass-dependent ion detection probabilities [39]. There, no closed form of a distribution function was found to describe the complete spectrum. In the present experiment, ions are accelerated by a potential difference of 18.55 kV (target potential 20 kV, detector potential 1.45 kV). This instrumental development was further essential for sensitive ion detection of biomolecules up to 500 000 u within the MALDI-TOF spectrometer used (Bruker Reflex III).

To confirm the accurate record of fullerene mass distributions, potential settings in the ion optical system of the linear detection mode have been varied in a proportionate way: (target, extraction electrode, einzel lens, MCP detector) (20.0, 18.6, 9.5, 1.45) kV, (16.0, 14.9, 7.8, 1.45) kV, (10.0, 9.4, 5.2, 1.45) kV. Thereby, a laser fluence of 0.9 J cm^{-2} was chosen for desorption. The reconstructed cumulative probability representations embrace the error band shown in figure 7. Here, the topmost and lowermost data points, respectively,

have been connected by straight lines. Fair agreement of all mass records has been obtained down to an acceleration voltage of (10.0–1.45) kV = 8.55 kV. This demonstrates that the cluster abundances, i.e. the distribution parameters, do not change significantly for the different potential settings and thus essentially reproduce the same measurement result quantitatively.

6. Conclusions

In the present work, a comparative study is presented demonstrating laser desorption/ionization mass distribution analysis of two different types of carbonaceous nanoparticle samples (i.e. nanodiamonds produced *ex situ*, fullerenes produced *in situ* during laser desorption/ionization from a carbon-rich target). Both samples reveal a lognormal size distribution function since the underlying growth process is of the same character, namely coalescent growth of arbitrary smaller particles to larger ones.

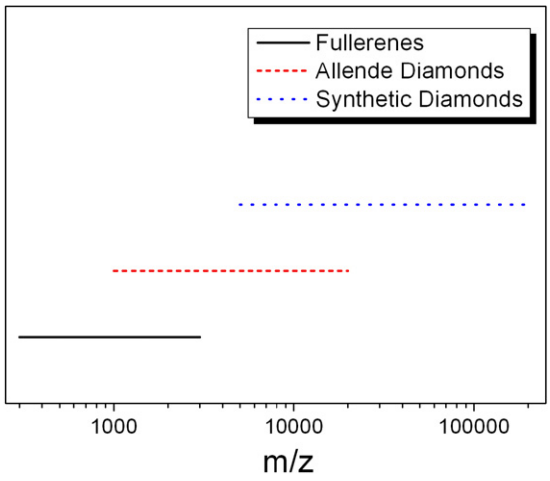

Figure 8. Overview of the approximate mass ranges embraced during laser desorption/ionization time-of-flight mass distribution analysis of the different types of carbonaceous nanoparticles.

The method presented allows for a quick analysis of nanoparticle mass distributions in a wide mass range, provided that the laser desorption process does not significantly disturb the nanoparticle properties. The variables implemented in such an analysis comprise, e.g., thermodynamic quantities like the growth temperature, the ambient pressure as well as growth rates. In case of fullerene ions, which are produced by the laser desorption process, the method could be used to observe growth in the real time domain.

Acknowledgments

The author would like to thank T Berg, G Huber, E Marosits, U Ott and Ch Sudek (Mainz) and J Höhndorf (Bruker Daltonia, Bremen) for collaboration and discussion during related work.

References

[1] Brus L 1991 *Appl. Phys.* **53** 465
[2] Hong Y-K *et al* 2002 *Appl. Phys. Lett.* **80** 884

[3] Ago H, Komatsu T, Ohshima S, Kuriki Y and Yumura M 2000 *Appl. Phys. Lett.* **77** 79
[4] Sun S, Murray C B, Weller D, Folks L and Moser A 2000 *Science* **287** 1989
[5] Klein D L, Roth R, Lim A K L, Alivisatos A P and McEuen P L 1997 *Nature* **389** 669
[6] Shim M and Guyot-Sionnest P 2000 *Nature* **407** 981
[7] Cui Y, Lauhon L J, Gudiksen M S, Wang J and Lieber C M 2001 *Appl. Phys. Lett.* **78** 2214
[8] Elia H-G 1990 *Makromoleküle* (Basel: Hüthig & Wepf)
[9] Swaminathan R, McHenry M E, Poddar P and Srikanth H 2005 *J. Appl. Phys.* **97** 10G104
[10] Rockenberger J, Nolting F, Lüning J, Hu J and Alivisatos A P 2002 *J. Chem. Phys.* **116** 6322
[11] Maul J *et al* 2004 *Nucl. Instrum. Methods* B **226** 644
[12] Kuznetsov V L, Chuvilin A L, Moroz E M, Kolomiichuk V N, Shaikhutdinov Sh K, Butenko Yu V and Mal'kov I Yu 1994 *Carbon* **32** 873
[13] Anders E and Zinner E 1993 *Meteoritics* **28** 490
[14] Cassat P, Muller J F, Manuelli P, Vichot A and Colombet P 1997 *Rapid Commun. Mass Spectrom.* **11** 1612
[15] Lewis R E, Anders E and Draine B T 1989 *Nature* **339** 117
[16] Maul J, Marosits E, Sudek Ch, Berg T and Ott U 2005 *Phys. Rev.* B **72** 245401
[17] Aitchison J and Brown J A C 1969 *The Lognormal Distribution* (Cambridge: Cambridge University Press)
[18] Hastings N A J and Peacock J B 1975 *Statistical Distributions* (London: Butterworths)
[19] Daulton T L, Eisenhour D D, Bernatowicz T J, Lewis R S and Buseck P R 1996 *Geochim. Cosmochim. Acta* **60** 4853
[20] Fraundorf Ph, Fraundorf G, Bernatowicz T, Lewis R and Tang M 1989 *Ultramicroscopy* **27** 401
[21] Lyon I 2005 *Meteorit. Planet. Sci.* **40** 981
[22] Whitehouse C M, Dryer R N, Yamashita M and Fenn J B 1988 *Anal. Chem.* **57** 675
[23] Räder H J and Schrepp W 1998 *Acta Polymer.* **49** 272
[24] Kroto H W 1987 *Nature* **329** 529
[25] Maul J, Berg T, Marosits E, Schönhense G and Huber G 2006 *Phys. Rev.* B **74** 161406(R)
[26] Wang C R, Huang R B, Liz Z Y and Zhend L S 1994 *Chem. Phys. Lett.* **227** 103
[27] McAlister D 1879 *Prog. R. Soc.* **29** 367
[28] Kile D E and Eberl D D 2003 *Am. Mineral.* **88** 1514
[29] Stein B *et al* 1994 *Geophys. Res. Lett.* **21** 1311
[30] Essery R, Li L and Pomeroy J 1999 *Hydrol. Proc.* **13** 2423
[31] Creasy W R 1990 *J. Chem. Phys.* **92** 7223
[32] Creasy W R and Brenna J T 1990 *J. Chem. Phys.* **92** 2269
[33] Villarica M, Casey M J, Goodisman J and Chaiken J 1993 *J. Chem. Phys.* **98** 4610
[34] Smoluchowski Mv 1916 *Phys. Z.* **17** 557
[35] Russo R E, Mao X and Mao S S 2002 *Anal. Chem.* **71A** 74
[36] Hieftje G M *et al* 1997 *J. Anal. At. Spectrom.* **12** 287
[37] Wiza J L 1979 *Nucl. Instrum. Methods* **162** 587
[38] Oberheide J, Wilhelms P and Zimmer M 1999 *Meas. Sci. Technol.* **8** 351
[39] Campbell E E B, Ulmer G, Hasselberger B, Busmann H G and Hertel I V 1990 *J. Chem. Phys.* **93** 6900